Journal of The Electrochemical Society, **157** (7) B1081-B1093 (2010)
0013-4651/2010/157(7)/B1081/13/$28.00 © The Electrochemical Society

Nitrogen Front Evolution in Purged Polymer Electrolyte Membrane Fuel Cell with Dead-Ended Anode

Jason B. Siegel,[a,*,z] Stanislav V. Bohac,[b] Anna G. Stefanopoulou,[b] and Serhat Yesilyurt[c]

[a]*Electrical Engineering and Computer Science, and* [b]*Mechanical Engineering, University of Michigan, Ann Arbor, Michigan 48109, USA*
[c]*Sabancı University, Orhanli-Tuzla, 34956 Istanbul, Turkey*

In this paper, we model and experimentally verify the evolution of liquid water and nitrogen fronts along the length of the anode channel in a proton exchange membrane fuel cell operating with a dead-ended anode that is fed by dry hydrogen. The accumulation of inert nitrogen and liquid water in the anode causes a voltage drop, which is recoverable by purging the anode. Experiments were designed to clarify the effect of N_2 blanketing, water plugging of the channels, and flooding of the gas diffusion layer. The observation of each phenomenon is facilitated by simultaneous gas chromatography measurements on samples extracted from the anode channel to measure the nitrogen content and neutron imaging to measure the liquid water distribution. A model of the accumulation is presented, which describes the dynamic evolution of a N_2 blanketing front in the anode channel leading to the development of a hydrogen starved region. The prediction of the voltage drop between purge cycles during nonwater plugging channel conditions is shown. The model is capable of describing both the two-sloped behavior of the voltage decay and the time at which the steeper slope begins by capturing the effect of H_2 concentration loss and the area of the H_2 starved region along the anode channel.
 [DOI: 10.1149/1.3425743]

Manuscript submitted March 8, 2010; revised manuscript received April 12, 2010. Published May 27, 2010.

The dynamic behavior of fuel cell (FC) operation under dead-ended anode (DEA) conditions are modeled and measured in this paper. Although a flow-through operation is used on both the anode and cathode of most laboratory/experimental hydrogen proton exchange membrane fuel cell (PEMFC) systems, the fuel utilization of the anode flow-through operation is too low for commercial and portable systems. To increase the flow-through utilization, anode recirculation is employed but the required hydrogen grade plumbing and hardware (ejector/blower) adds weight, volume, and expense to the system.[1,2] Additional complexity is also added to the balance of plant with the use of external humidification to prevent overdrying of the membrane. However, a DEA can be fed with dry hydrogen, which is regulated to maintain anode pressure. In this configuration, hydrogen is supplied at exactly the rate needed to support the reaction. FC operation with dry hydrogen in a dead-ended system architecture is possible because water crossing through the membrane is enough to humidify the fuel. The use of a pressure regulator instead of a mass flow controller and lack of anode inlet humidification can yield a system with lower cost and weight.

The only problem with this architecture is that nitrogen, from air fed into the cathode, can also cross the membrane, driven by the gradient in partial pressure, creating a blanket of N_2. Water vapor gradients between the humidified cathode and the dry fed anode also drives excess water into the anode, which can cause significant liquid water accumulation. Unlike water vapor whose maximum partial volume is dictated by temperature, liquid can fill the entire free space and block the flow of reactants, also known as channel plugging. The accumulation of liquid water and nitrogen in the anode channel (AN CH) is first observed near the outlet of the channel. Both gravity and gas velocity driven by consumption of hydrogen pull these heavier molecules toward the bottom of the channel. As the mass accumulation continues, a stratified pattern, which is stabilized by the effect of gravity, develops in the channel with a hydrogen-rich area sitting above a hydrogen depleted region. The boundary between these regions is a time-varying front, which proceeds upward toward the inlet.[3] The mass accumulation physically blocks hydrogen gas from reaching the anode catalyst sites, which is the mechanism for the experimentally observed and recoverable voltage degradation.[4-6] We propose that the accumulation of N_2 and H_2O initially leads to larger concentration losses due to decreasing hydrogen concentration near the bottom of the AN CH. When a critical amount of N_2 accumulates in the channel, it completely blocks H_2 from reaching the catalyst, effectively shrinking the active area of the cell causing larger activation potential in the cathode. This two-stage mechanism is clearly visible in all experimental conditions and scales with operating conditions such as load current density, relative humidity (RH), and stoichiometric ratio (SR) in the cathode.

Purges of the AN CH volume are necessary to clear the reaction product and inert gas from the channel. An anode purge event consists of opening a downstream solenoid valve, which creates a brief, high velocity flow-through the anode, removing liquid water and nitrogen. After the purge, the catalyst area contributing to the reaction increases and, hence, the measured voltage increases. Understanding, modeling, and predicting the front evolution and overall dynamics in DEA FC would allow judicious choice of purging interval and duration. Better purging strategy can reduce the H_2 wasted during purges and avoid overdrying the membrane. The operation of a PEMFC with hydrogen starved areas can also lead to carbon corrosion;[7-9] therefore, the study of these operating conditions and the derivation of controllers to schedule anode purges are critical for DEA operation and prolonging stack life.

For a fixed purge period and duration, the FC reaches a stable cyclic behavior, typically within a few purge periods, with both consistently repeatable voltage degradation rates between purges and voltage recovery with each purge. We verified the repeatability of the front evolution with in situ neutron imaging, measuring the liquid water front, and gas chromatography (GC), measuring the hydrogen and nitrogen concentrations at a specific location in the AN CH, as shown in Fig. 1, which is discussed later. Gravity, buoyancy, and channel orientation help establish these statistically repeatable and large spatiotemporal variations with hydrogen starvation fronts. Figure 2 shows typical spatial and temporal patterns of liquid water thickness and associated measurements during DEA operation with infrequent anode purging events. The stratification of the hydrogen/nitrogen fronts and the gravity-driven liquid water in the channels also provide a unique modeling paradigm and distinct conditions augmenting an earlier work[6,10-14] that has not been studied extensively before despite several strictly experimental results.[15-17]

This paper elucidates the DEA hydrogen PEMFC behavior; specifically, we first introduce the experimental setup, examine the data, and then propose a simple along-the-channel model. We use the model to explain the observed voltage behavior during DEA operation. Because accumulation of both liquid water and nitrogen in the

* Electrochemical Society Student Member.
[z] E-mail: siegeljb@umich.edu

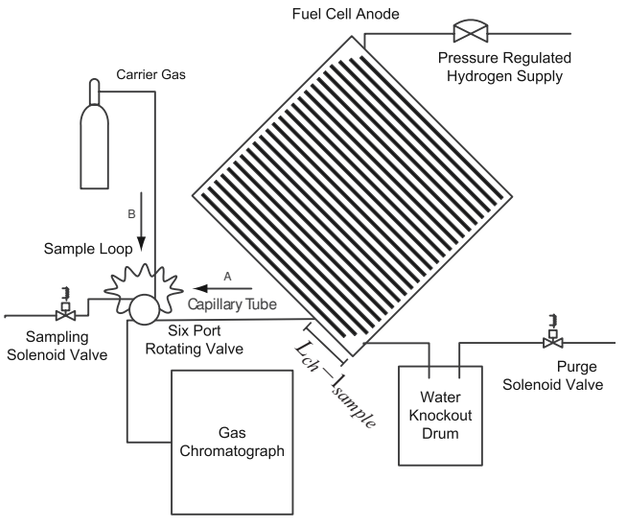

Figure 1. Illustration of anode flow-field orientation and GC setup with six-port rotating valve. In position A, the flow-through of the SL is from right to left, the FC is connected to the SL and SV, whereas the carrier gas flows to the GC. In position B, the flow-through of the SL is from top to bottom, the carrier gas is connected to the SL and GC, whereas the FC is connected to the SV.

AN CH of a PEMFC operating under dead-ended conditions contribute to the recoverable voltage degradation, we devised experiments to characterize the relative effects of both constituents using simultaneous in situ measurements of both nitrogen and liquid water. Anode purges and cathode surges when coupled with voltage measurement can be used as a diagnostic tool for determining the location of water flooding and the impact of nitrogen blanketing in the AN CH. An anode purge, which is a short duration, high flow rate of gas though the anode initiated by opening a downstream valve, removes both liquid water and nitrogen gas from the AN CH and recovers the voltage drop caused by a reduced active area on the anode side. A cathode surge is a momentary increase in the air flow rate supplied to the cathode. The excess air increases the partial pressure of oxygen in the channel, which leads to increased voltage for the duration of the surge. The excess air flow rate can also remove water from the cathode channel (CA CH) and cathode GDL, which leads to an improvement of the FC voltage after the surge relative to the value before initiating the surge.

Finally, we compare the data with a model that captures the relative impact of each process on the measured cell voltage. In Ref. 3, the effects of nitrogen accumulation driven by convection were investigated, which we improve upon this work by inclusion of diffusive terms in the AN CH and a physics based voltage model, which accounts for membrane water content with a distributed current density. By correlating measurements of voltage, liquid water mass, and AN CH gas concentration, we aim to develop and validate a model of PEMFC under DEA operating conditions. Once properly calibrated, this model can be used for anode purge scheduling and stack health monitoring. Snapshots of the data are presented to demonstrate the repeatability of the observed phenomena and to provide comparisons with the model. To prevent confusion and clarify the observed phenomena, the term flooding is used to describe the accumulation of liquid water in the GDL or catalyst layer, and the term plugging is used to refer to liquid water in the channels, which blocks or hinders the flow of gas through the channels.[18] The term blanketing is used to designate N_2 mass accumulation in the AN CH, which prevents hydrogen from reaching the catalyst layer.

Experimental Setup

A Shimadzu GC-17A gas chromatograph was used to measure the hydrogen, nitrogen, and oxygen content of gas samples taken from the AN CH of a PEMFC during dead-ended operation. Simultaneous measurement of the liquid water distribution inside the FC was acquired via neutron imaging at the National Institute for Standards and Technology in Gaithersburg, MD.[6,19]

Configuration and operating conditions.— The tested FC had an active area of 50 cm^2. The anode gas flow path consisted of 25 parallel straight channels with a depth of 1.78 mm and a width of 2.08 mm. The anode land width was 0.838 mm, and the channel length was 7.3 cm. The AN CHs were oriented on a 45° angle and connected at the top and bottom of each channel by a manifold, as shown in Fig. 1. A supply of dry pressure regulated hydrogen at 4.5 psig was fed to the DEA. As hydrogen was consumed in the reaction, the pressure regulator maintained constant pressure in the AN CH, effectively maintaining operation at hydrogen utilization of one. A solenoid valve located downstream of the FC anode can be periodically opened to purge the anode volume, as shown in Fig. 1. This valve was referred to as the purge valve (PV). An adjustable valve is located downstream from the anode PV to reduce the pressure drop and flow during a purge. The valve was adjusted before starting the experiment and remained fixed. The steady-state flow rate during purging was measured to be ~1 slpm of hydrogen. The value (N_{purge}) listed in Table I was used to model this outlet flow. Due to the small diameter passageway between the AN CHs and the outlet manifold of the FC, liquid water may impede the flow of gases during the initial portion of a purge. Another solenoid valve was located downstream, connected by capillary tubing, to allow gas sampling from the AN CH. This solenoid valve was referred to as the sampling valve (SV) and is described in the gas chromatography setup section. A microcontroller was used to actuate the solenoid valves precisely in time and control the purge event period and duration.

A traditional flow-through architecture with air was used on the cathode side with a bubbler-type humidifier. A backpressure regulator downstream from the cathode maintained the pressure between 3.5 and 4.5 psig depending on the flow rate. The CA CHs had a nine-pass semiserpentine flow path consisting of five parallel channels. Typical cathode flow rates ranged from SR 1.5–3 (oxygen supplied/oxygen consumed). Due to the use of air on the cathode, the gas velocities in the channel were much higher than a system running on pure oxygen at the same SR. The RH of the gas stream was varied between 50 and 100%. Cathode surges, which are short duration (1–2 s) increases in the air flow rate (up to SR 10), were used during the experiment to remove liquid water from the CA CHs and to diagnose the extent of CA CH plugging. The cathode flow field was aligned perpendicular to the AN CHs, but the inlets and outlets were colocated at the upper and lower corners of the cell, respectively. As a result, the system behavior can be approximated by an equivalent coflow model, as discussed in the Modeling section.

GC setup.— The setup shown in Fig. 1 illustrates the interconnection of the GC equipment and FC. A heated capillary tube was inserted into the last AN CH (near the edge of the cell), 3 cm from the bottom corner, as shown in Fig. 1. The 0.005 in. diameter capillary tube was connected to an electrically actuated six-port rotational valve. The SV was placed downstream from the six-port valve which, when opened, allows for filling of the sample loop (SL) from the FC AN CH when the six-port valve is in position A. After a sample was collected in the SL and the SV was closed, the six-port valve was rotated to position B, and the high pressure carrier gas (helium) pushed the sample into the GC for analysis.

Ultrahigh purity helium was used as the carrier gas and supplied at a pressure of 200 kPa gauge. This produced a steady flow of 12 mL/min to the GC. A thermal conductivity detector (TCD) was used for gas detection. As a result of the choice of column (Heyesep D

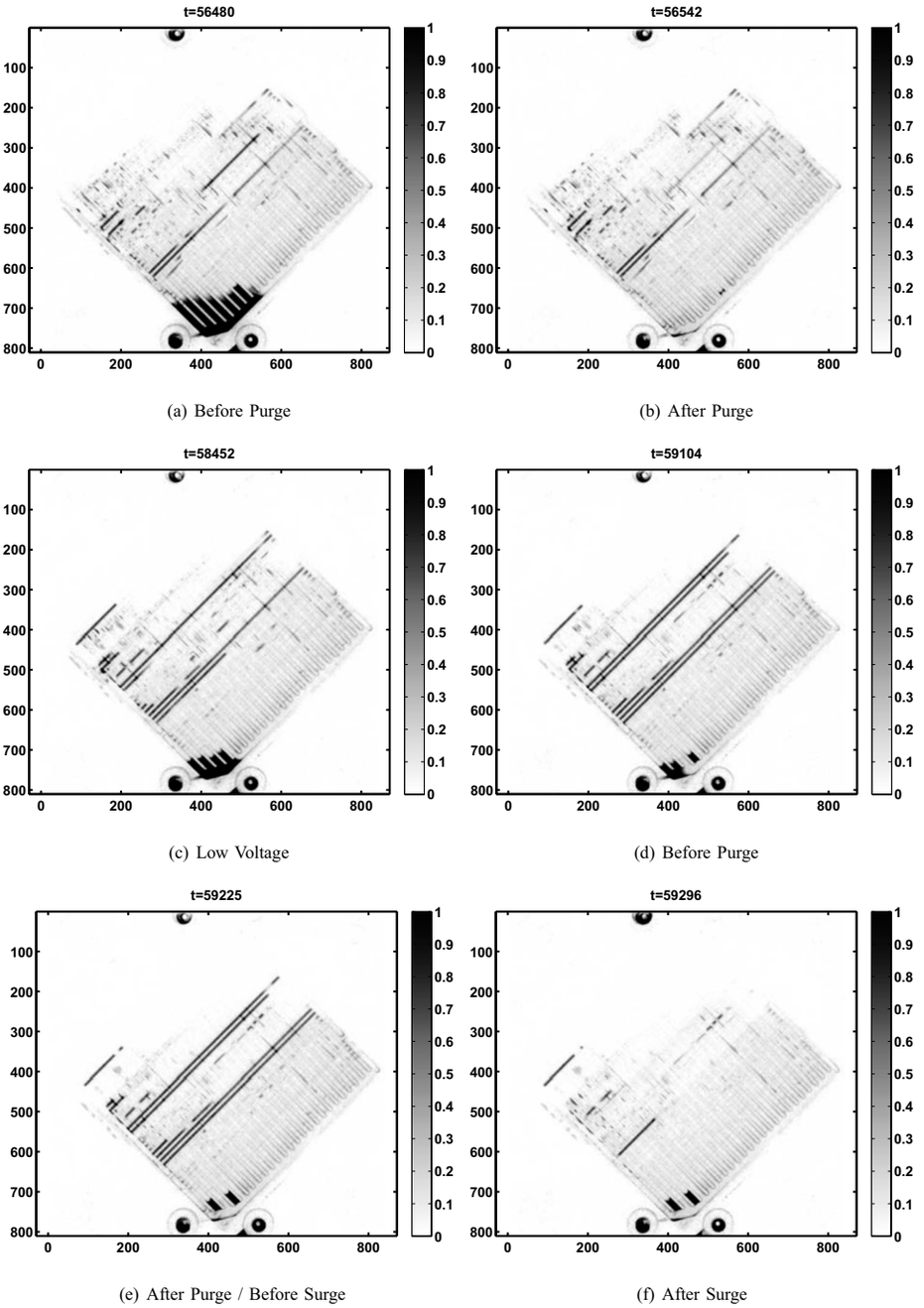

(a) Before Purge (b) After Purge

(c) Low Voltage (d) Before Purge

(e) After Purge / Before Surge (f) After Surge

Figure 2. Neutron images.

column Restek, 100/120 mesh, 3 m length, 1 mm inner diameter), the measurement of water vapor was not possible due to the very long elution time for water in the column. The difference in retention times of the GC for hydrogen and nitrogen measurement constrained the maximum sampling rate at one sample every 40 s. The SV was opened for 1 s, during which ~300 μL of gas was removed from the AN CH (hence, the sample volume was less than 5% of the total anode volume). The total anode volume was 6500 μL. Only the last 5 μL of the sample was trapped in the SL and then pushed into the GC when the six-port valve was rotated. The capillary tubing, six-port SV, and SL were maintained at a constant temperature of 110°C to ensure that a consistent sample concentration was delivered to the GC and to prevent condensation in the tubing. Details on the GC calibration can be found in the Appendix.

Neutron radiography.— Neutron radiography is an in situ, nondestructive test that involves placing the FC in a beam of neutrons and measuring the change in beam intensity as it passes through the FC. The decrease in beam intensity is caused primarily by neutron interaction with liquid water in the FC. By comparing the image intensity with that of a known dry FC, the two-dimensional (2D) distribution of liquid water thickness values in the plane perpendicular to the beam can be calculated.[6,20] Six of these processed images, showing water thickness values in millimeters, are presented in Fig. 2, where the images were selected from the data set shown in Fig. 3. Figure 2a and b clearly shows AN CH water accumulation and the effectiveness of the anode purge in removing water from the channel. Figure 2e and f shows the effect of cathode surge at removing water from plugged CA CHs. Figure 2c and d shows the small

Table I. Constants.

E_{N_2}	24,000 J mol^{-1}	39
T_{ref}	303 (K)	39
R	8.314	Universal gas constant
V_w	1.81×10^{-5}	Water volume[26]
V_{mb}	5.59×10^{-4}	Membrane volume[26]
K_{mb}	0.25	Membrane water uptake
n	2	Electron transfer number
F	96,485 C mol^{-1}	Faraday's constant
C_{ref,O_2}	40.87 mol m^{-3}	
C_{ref,H_2}	40.87 mol m^{-3}	
E_c	66,000 J mol^{-1}	30
T_0	298.15 K	Reference temperature
$\alpha_{a,a}$	0.5	
$\alpha_{c,a}$	0.5	
D_{12}	2.56×10^{-6} m^2 s^{-1}	D_{H_2O,N_2} [25]
D_{13}	8.33×10^{-6} m^2 s^{-1}	D_{H_2,N_2} [42]
D_{23}	9.15×10^{-6} m^2 s^{-1}	D_{H_2O,H_2} [25]
$w_{an,ch}$	0.0021 m	AN CH width
$w_{an,rib}$	8.38×10^{-4} m	Anode rib width
Δ_{mb}	25 μm	Membrane thickness
$h_{an,ch}$	0.0018 m	AN CH height
L_{ch}	0.0727 m	Channel length
Δ_{GDL}	3.36×10^{-4} m	Compressed GDL thickness
N_{sample}	9.2×10^{-7} mol s^{-1}	Sample flow rate
N_{purge}	5×10^{-3} mol s^{-1}	Purge flow rate

reduction of the AN CH water plugging, which occurred during repeated anode sampling. During this period, the voltage continuously improved, as shown in Fig. 3, which was the combined effect of nitrogen and liquid water removal from the channel. Nitrogen was removed with the gas sample, and liquid water droplets were dislodged by the pressure variations in the channel due to the sampling and fell to the bottom of the channel via gravity.

The time-series sequence of neutron images were further processed in two ways so that the amount of data was reduced and the relevant features were easier to visualize over time. The first method of data reduction was to estimate the total liquid water mass in each of the three layers, the CA CH, AN CH, and the combined membrane/GDL sandwich layer, by comparing the local water distributions corresponding to the different combinations of channels and lands, as described in Ref. 6. These values are shown in the fifth and sixth subplots of Fig. 3 and 4 and help identify the presence of GDL water flooding or channel water plugging. To make an inference about the channel water mass from the 2D projection of water distribution in the FC, we must assume that locally the GDL water content was uniform in the rib and channel areas. If this assumption is not valid, the algorithm used overestimates the GDL water content (attributing too much of the measured water mass to the GDL) and underestimates the channel water content especially in the cathode GDL because computational fluid dynamic models have demonstrated water accumulation to be greater under the ribs[21] for single serpentine coflow channels under certain operating conditions. Another plausible scenario is that the high gas flow rate in the CA CH could have a Venturi effect, drawing liquid from the GDL, when the water saturation is above the immobile limit, which could explain the correlation in water removal. It was not possible to determine if the correlation (a decrease in total water masses) between the GDL and CA CH during a surge, as shown in Fig. 3 at $t = 3400$ s, was physical or an artifact, given the present set of measurements. Future work, using neutron imaging with the beam direction parallel to the membrane, will be used to investigate the relationship between GDL and channel liquid water removal. This uncertainty in the location of water accumulation did not impact the nitrogen accumulation or voltage degradation rates measured or modeled in this paper, and we have chosen conditions with less channel water accumulation for model validation.

The second method of analysis quantifies the fractional area coverage by liquid water and is shown in the seventh subplot of Fig. 3 and 4. Hence, the image processing provides information for (a) the total liquid water mass, which is a volume average along the path of the beam at a specific time and (b) information about the distribution of water within the FC, specifically the membrane area that is exposed to liquid water. This additional information is important for modeling because of the difference in membrane properties, proton conductivity, and permeation rate, as a function of membrane water content. The fractional area coverage was calculated for two different water thickness values: Water thickness values greater than 0.3 mm indicate the presence of water in the channels, and water thickness greater than 0.05 mm are chosen to indicate the start of GDL hydration, which also indicates an area with higher membrane water content.

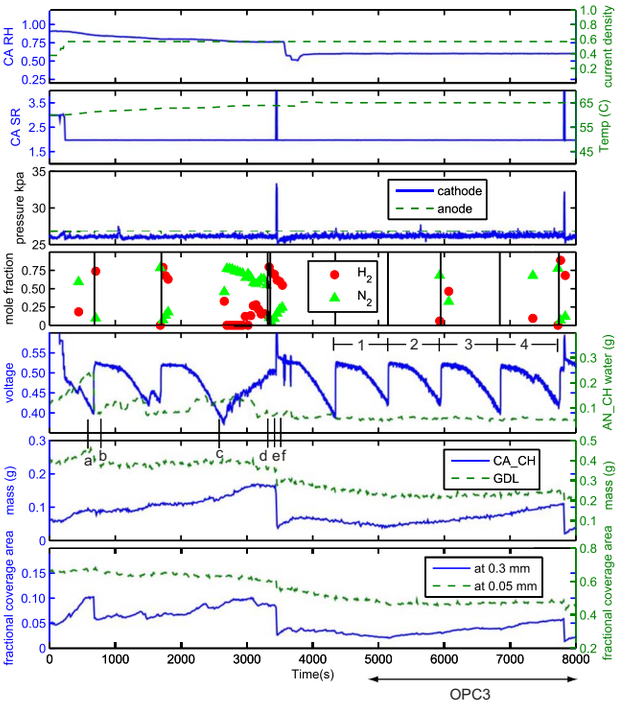

Figure 3. (Color online) Operating conditions and processed liquid water data from neutron images, corresponding to initial experiment time $t_0 = 55{,}800$ s. The dashed lines correspond to the axis on the right, and solid lines use the left axis. The top subplot shows CA RH as a fraction (0–1) (solid lines) and current density (A cm^{-2}) (dashed lines). The second subplot shows CA SR (solid lines) and cell temperature (°C) (dashed lines). The third subplot shows cathode (solid lines) and AN CH pressure (kPa gauge) (dashed lines). The fourth subplot shows the mole fraction of hydrogen and nitrogen that was measured from GC sampling, and the vertical lines indicate anode purge events. The fifth subplot shows the cell voltage (solid lines) and the estimated mass of liquid water in the AN CH (dashed lines). (a)-(f) indicate the times at which neutron images (a)-(f) in Fig. 2 were acquired. The sixth subplot shows the estimated CA CH liquid water mass (solid lines) and GDL mass (g) (dashed lines). Finally, the seventh subplot shows the fractional FC area from neutron imaging, with a measured liquid water thickness greater than 0.3 or 0.05 mm.

Experimental Results

The data listed in Fig. 3 and 4 represent the dynamic responses of a PEMFC; there are changes in air flow, current density, cathode inlet RH, and temperature, as indicated in the upper subplots of these figures. In the time period before what is shown in Fig. 3, the FC was operated for several hours at 55°C, with a low current density (0.2 and 0.4 A cm^{-2}) and a fully humidified cathode inlet. The data in Fig. 4 follow Fig. 3 after the cell was dried at 50% cathode inlet RH for 1 h.

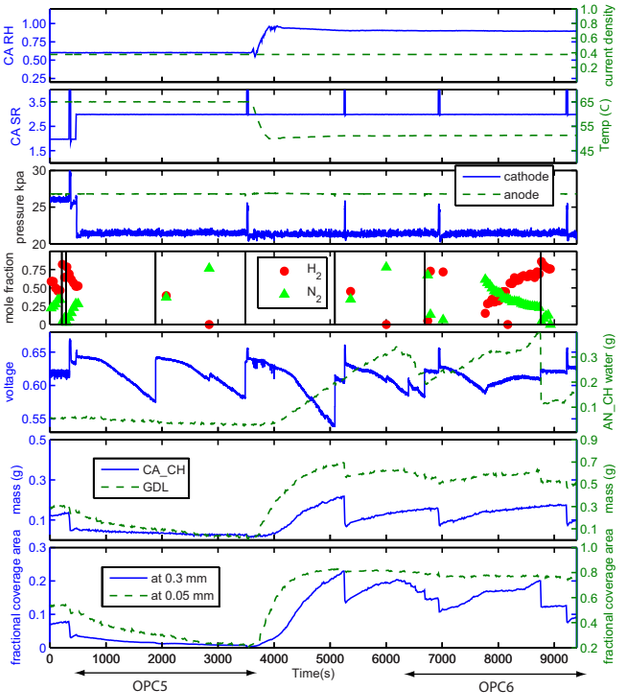

Figure 4. (Color online) Selected data set 2 beginning at $t_0 = 67,800$ s, which shows the transition from subsaturated cathode inlet conditions to fully humidified conditions and the onset of channel plugging.

The repeatable and recoverable voltage decay, which is caused by mass accumulation in the anode, can be seen in the voltage plot, with the solid line type in the fifth subplot of Fig. 3 and 4. The anode purge events indicated by the black vertical lines in the fourth subplot precede each of the largest voltage improvements. Cathode surges are also correlated with voltage improvement, as discussed in the following section.

An important feature of the observed voltage dynamic is the two-sloped decay. A slow initial decay, which can be attributed to the dilution of hydrogen in the anode, is followed by a steeper linear decay, which marks the development of a hydrogen depleted region that is covered by a blanketing N_2 front moving upward toward the inlet. Various operating conditions are selected to demonstrate the complex phenomena occurring during the DEA operation.

Table II summarizes the operating conditions depicted in the following figures and discussion. The operating conditions are described using the following notation: (i # _ T # _ SR # _ RH#),

Table II. Select cases from data set for model comparison.

RH/SR	Low (2)	High (3)
	$T = 50°C$	
Full	[1], 8	[6], (7)
Mid		
	$T = 60°C$	
Full	11	[2], (9), [10]
Mid		
	$T = 65°C$	
Full		
Mid	3, [4]	[5]

OPC x	Current density
(x)	0.2 A cm^{-2}
[x]	0.4 A cm^{-2}
x	0.6 A cm^{-2}

where the number following i denotes the current density in A cm^{-2}, T represents temperature (°C), SR is the cathode stoichiometry, and RH is the cathode inlet RH. The data sets are available online at http://orion.engin.umich.edu.

Both N_2 blanketing and liquid water plugging could displace H_2, preventing it from reaching the catalyst sites. To study the relative effects of both constituents, we identify portions of the data set corresponding to conditions with and without anode water accumulation. In this work, lower cathode inlet RH (60%) cases are used for the investigation of a single phase channel model; hence, the influence of N_2 accumulation on voltage can be separately identified. The lack of AN CH plugging is verified from the neutron radiography data.

The operating conditions for case 5 are (i0.4 _ T60 _ SR3 _ RH60), as shown in Table II, which are medium current density, 60°C, and high flow rate of subsaturated air supplied to the cathode. This case is shown in Fig. 4 and is chosen to represent a single phase condition for model comparison in the Modeling results section.

Cathode surges vs anode purges.— In the DEA operation of PEMFCs, anode purges and cathode surges, when coupled with voltage measurement, can be used as a diagnostic tool for determining the location of water flooding and the impact of nitrogen blanketing in the AN CH. An anode purge, which is a short duration, high flow rate of gas through the anode initiated by opening the PV, removes both liquid water and nitrogen gas from the AN CH and recovers the voltage drop caused by the reduced active area on the anode side. A representative section of our experiments is shown in Fig. 3. The first anode purge at $t = 680$ s removes ~0.19 g of liquid water from the AN CH and the voltage improves by ~130 mV following the anode purge, as shown in the fifth subplot of Fig. 3. Neutron images from before (Fig. 2a), and after (Fig. 2b) the purge confirm the removal of liquid water from the AN CH.

A cathode surge is a momentary increase in the air flow rate supplied to the cathode. The excess air increases the partial pressure of oxygen in the channel, which leads to an increase in the measured cell voltage for the duration of the surge. The excess air flow rate also removes water from the CA CH and cathode GDL, which leads to an improvement of the FC voltage after the surge relative to the value before initiating the surge. This change in voltage should be related to the amount of water removed from the CA CH, GDL, or catalyst layer. Also, the resistance to O_2 transport between the channel and the cathode catalyst layer is reported to be large especially for carbon cloth GDLs,[22] and cathode purges effectively enhance the O_2 transport to those areas, especially under the rib. Cathode surges at $t = 3400$ s and $t = 7800$ s, indicated by the short duration spikes in the cathode stoichiometric ratio (CA SR) in the second subplot of Fig. 3, cause a temporary increase in cathode back-pressure and voltage during the duration of the surge, as shown in the third and fifth subplots of Fig. 3, respectively.

The surge at $t = 3700$ s recovers 36 mV of voltage, and the removal of liquid water from the CA CH can be clearly seen by comparing Fig. 2e from before the surge to Fig. 2f after. A larger voltage recovery from both surges and purges is expected at a high current density (0.6 A cm^{-2}), both because of the higher amount of cathode flooding and the greater effect the accumulated water has on voltage output because a higher local current density leads to lower overall electrochemical efficiency. The fractional coverage area at 0.3 mm, shown as the solid lines in the last subplot of Fig. 3, decreases with both anode purges and cathode surges that remove water from the channels because water thickness values above this threshold are attributed to channel accumulation. The estimates of channel water mass shown in the above subplots are well correlated with the surges, purges, and voltage recoveries.

Temperature effects.— The overall effect of temperature on FC voltage is difficult to quantify because temperature influences several competing factors. For example, an increased temperature leads

to faster reaction kinetics and increased proton conductivity, which both increase voltage. However, the increase in vapor pressure also decreases the oxygen partial pressure, which decreases voltage. So, the overall effect may be a decrease in voltage. Temperature also impacts the nitrogen crossover rate though the membrane. The nitrogen permeation rate, K_{N_2} in Eq. 30, increases exponentially with temperature. Saturation pressure also increases exponentially with temperature, so the partial pressure of water vapor is small at lower temperatures.

The slow decrease in cathode inlet RH, shown in Fig. 3, from $t = 200$ s to $t = 3200$ s following the increase in current density, can be attributed to the increased heat generation that leads to a higher cell temperature than the set point value (60°C), whereas the dew point of the inlet air stream remained constant. This subsaturated cathode air feed leads to a slight recession of the two-phase front location, as shown in the seventh subplot by the fractional coverage area, even though the decrease in CA SR keeps the gas velocity in the channel close to the previous value after considering the increase in current density.

Finally, the decrease in CA RH and increased cell temperature at the beginning at $t = 3800$ s leads to a more rapid drying of the FC.

The high temperature and low cathode inlet RH conditions shown in the first half of Fig. 4 lead to a dry condition within the FC. The total water mass is very low and the fractional water coverage is also low, indicating that the transition from subsaturated to saturated conditions along the length of the coflow channels is near the outlet. After the transition to lower cell temperature at $t = 3700$ s, which increases the cathode inlet RH from 60 to 100%, the two-phase front moves back toward the inlet, as indicated by the increase in the fractional area coverage (>0.05 mm). This leads to the onset of both AN CH plugging and CA CH plugging. When the channels are not plugged, the cathode surge at $t = 3500$ s has no sustained effect on voltage, but the surges following the increase to fully humidified cathode inlet conditions at $t = 5100$ s and $t = 7000$ s see voltage improvement that is well correlated with the water removal from the CA CH. Data indicate that GDL water accumulation (data points taken from under the lands) precedes the accumulation of water in the channels.

GC sampling effects.— The intent of GC sampling was to measure nitrogen accumulation in the AN CH. The measurement, however, modifies the system behavior. Specifically, the effect of GC sampling, that is, the removal of gas from the AN CH, can improve the FC voltage. When a sample removes accumulated nitrogen or water from near the end of the AN CH, it is replaced by a pure hydrogen flow from the inlet.

GC samples were initiated typically right before and after each purge event and sometimes in the middle of a purge period, as shown in the fourth subplot of Fig. 3. Individual GC sampling events are correlated with the small voltage increases shown in the fifth subplot of Fig. 3. A series of samples, between $t = 2700$ and 3500 s, was taken at the fastest sampling rate of the GC detector.

The effect of sampling has more impact on voltage with increasing time since the last anode purge event. This can be explained by the nitrogen accumulation model presented in the Modeling section. Samples taken from later in the cycle allow more nitrogen to accumulate in the AN CH, see for example the sample taken at $t = 350$ s in Fig. 3. If nitrogen does not have sufficient time to accumulate, the sample removes primarily hydrogen from the channel and no voltage improvement is observed, see for example the sample taken at $t = 700$ s immediately following an anode purge.

The continuous sampling, at one sample every 40 s, observed between $t = 2700$ and 3500 s in Fig. 3, is responsible for the voltage recovery observed over that time interval. If the sampling rate is fast enough to remove more volume than the amount of nitrogen that crosses over through the membrane in that time, then the measured voltage increases with each subsequent sample. The fluctuations in anode pressure, due to the repeated sampling, also enhance liquid water removal from the AN CH by allowing liquid water to escape from the channel into the outlet manifold. During normal operation, the outlet manifold is at the same pressure at the channel, so there is no flow between these volumes. This explains the drop in AN CH liquid water mass observed between Fig. 2c and d.

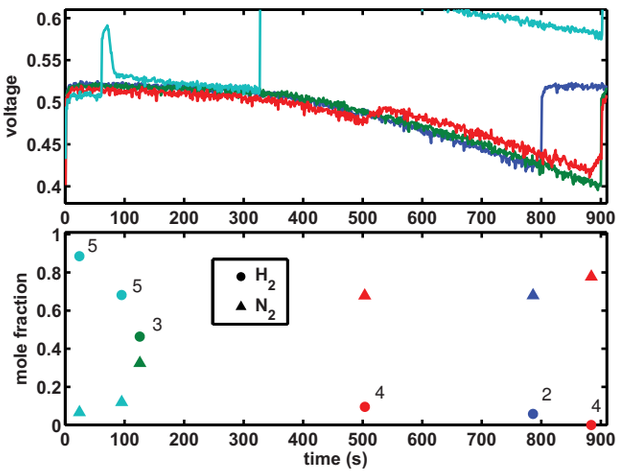

Figure 5. (Color online) Subsequent purge cycles are plotted vs time since the previous purge. The data corresponds to operating condition 3 from the larger data set shown in Fig. 3. The numbers 1–5 on the bottom subplot indicate during which purge cycle each GC sample was taken.

Voltage repeatability.— The repeatability of several purge cycles, from the end of the larger data set shown in Fig. 3, can be seen by plotting each cycle vs the time since the previous purge, as shown in Fig. 5, creating an overlay of the voltage decays with time. The repeatability of the voltage decay characteristics between cycles is remarkable, given the fact that some purge cycles contain surge events. Similarly, the repeatability and consistency of the measured mole fractions every purge cycle is very important for modeling and understanding the underlying phenomena. This analysis is useful, considering the impact of GC sampling on voltage and nitrogen distribution in the AN CH. The composition of several samples from different points in time during the purge cycle and from different cycles allows us to form an accurate representation of nitrogen accumulation and voltage decay. Notice that the nitrogen mole fraction, shown in the bottom subplot of Fig. 5, saturates at around 0.8; the remaining 20% of the gas is saturated water vapor in the AN CH.

Modeling

In this section, a one-dimensional model of nitrogen crossover and accumulation in the AN CH of a DEA PEMFC is presented. The modeling domain for this work is the AN CH and membrane. Nitrogen crossing though the membrane into the AN CH is pushed to the end of the channel by the convective velocity.[3] The convective velocity is the result of hydrogen consumption and, therefore, the velocity is greatest near the anode inlet, decreasing along the length of the channel. Due to the high diffusivity of hydrogen in the AN CH, we use the Stefan–Maxwell equation to describe the nitrogen distribution along the channel, resulting from both convection and diffusion, for comparison with the measured mole fractions from GC sampling. A physics based voltage model is used to account for the distributed current density and hydrogen consumption rate. The voltage model includes the effect of membrane water content and proton concentration. We consider an isothermal modeling approach, and the measured cell end plate temperature is used for T.

The important dimensions for channel modeling are x, the through-membrane direction, and y, the along-the-channel direction, as shown in Fig. 6. For the anode, the spatial variation of gas concentrations in the x-direction is considered, but the steady-state gas diffusion profiles are calculated and used to propagate the channel

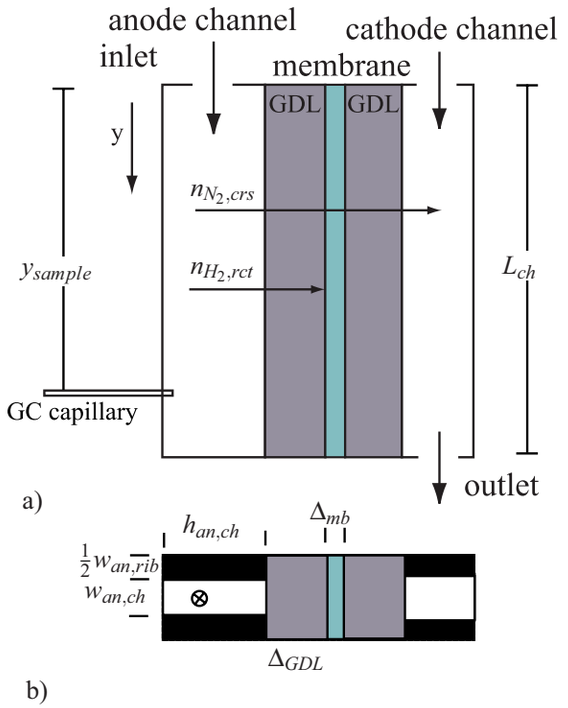

Figure 6. (Color online) (a) One-dimensional FC modeling domain; y denotes the distance along the channel from inlet to outlet (not drawn to scale). (b) FC channel dimensions.

values (which are modeled as dynamic states) across the GDL to the surface of the membrane. A similar decoupling between the x and y distributions is proposed in Ref. 23 to address the computational complexity and to take advantage of the very different length scales. On the cathode, only the steady-state profiles are considered for modeling both the x- and y-dimensions. The approximation of steady-state distributions is appropriate for the cathode gas channel due to the high gas flow rate and the large time scales over which the anode dynamics evolve.

The constants, listed in Table I, and equations describing the gas constituents in the channels are written using SI units. The exceptions are the related parameters in the voltage model (Table III), which use A cm^{-2} consistent with the FC literature. In the along-the-channel model, the fluxes n have units (mol m^{-1} s^{-1}) and flows N (mol s^{-1}).

Nitrogen accumulation (single phase along the channel model).— To consider both water and nitrogen transport though the membrane, our modeling effort requires consideration of a ternary system for the anode. The Stefan–Maxwell model describes convection, diffusion, and reactions in the gas channel

$$\frac{P_{an}}{RT}\frac{\partial x_i}{\partial t} = -\frac{\partial}{\partial y}(J_i + x_i N_t) + r_i \qquad [1]$$

for $i = [1,2]$, where N_t is the total gas flux, J_i is the diffusive flux, and r_i denotes the reaction terms. Only two of the three components are independent in this modeling framework. We chose the mole fractions of nitrogen, $x_{N_2} = x_1$, and water vapor, $x_{H_2O} = x_2$, as our dynamics states. Because the mole fractions must sum to one

$$\sum x_i = 1 \qquad [2]$$

we can calculate the hydrogen from the other gases $x_{H_2}(y) = 1 - x_{N_2}(y) - x_{H_2O}(y)$. $x_{H_2} = \min(x_2, P_{sat}(T)/P_{an,in})$ is used for all the following calculations, including J_i. The remaining water is assumed to be liquid water and is tracked separately; we are assuming instant condensation.

The convective flux N_t is driven by the consumption of hydrogen (Eq. 7). In Eq. 1, a constant pressure is used as an approximation because the anode volume is fed via pressure regulation and the straight channel geometry introduces minimal pressure drop along the length of the channel. Although a pressure gradient, corresponding to the convective flux, develops along the length of the channel, the pressure drop is less than 1 Pa at 1 A cm^{-2}, so a constant pressure is valid for calculating the concentrations. The ideal gas law, PV = nRT or $P = cRT$, is used to relate pressure and mole fraction of gas species in the channel.

A causal formulation for the diffusive fluxes is used[24]

$$\begin{bmatrix} J_1 \\ J_2 \end{bmatrix} = -\frac{P_{an}}{RT\phi(x)}\begin{bmatrix} D_1(x_1), & D_2(x_1) \\ D_3(x_2), & D_4(x_2) \end{bmatrix}\begin{bmatrix} \frac{\partial x_1}{\partial y} \\ \frac{\partial x_2}{\partial y} \end{bmatrix} \qquad [3]$$

where

$$D_1(x_1) = (1 - x_1)D_{13}D_{12} + x_1 D_{23}D_{13}$$

$$D_2(x_1) = -x_1(D_{23}D_{12} - D_{23}D_{13})$$

$$D_3(x_2) = -x_2(D_{13}D_{12} - D_{23}D_{13})$$

$$D_4(x_2) = (1 - x_2)D_{23}D_{12} + x_2 D_{23}D_{13} \qquad [4]$$

and D_{ij} are the temperature-dependent binary diffusion coefficients from Ref. 25. $\phi(x)$ is given by

$$\phi(x) = (D_{23} - D_{12})x_1 + (D_{13} - D_{12})x_2 \qquad [5]$$

Conservation of mass allows solving of Eq. 1 for $N_t(y)$, assuming the outlet flow is known $N_t(L) = N_{out}$. The equation for conservation of mass can be written as

$$\frac{\partial N_t}{\partial y} = \sum r_i \qquad [6]$$

because $\Sigma J_i = 0$ by definition. Then the convective flux along the channel can be found from Eq. 6 by integrating backward in space along the channel

$$N_t(y) = N_t(L) + \int_y^L [n_{H_2,rct}(\tilde{y}) + n_{N_2,crs}(\tilde{y}) + n_{H_2O,crs}(\tilde{y})]d\tilde{y} \qquad [7]$$

Because the anode is dead-ended, $N_{out} = 0$ unless the downstream solenoid valve is open and the anode is purging, in which case $N_{out} = N_{purge}$, a constant.

The source term for nitrogen in the AN CH is membrane crossover, which is calculated from the difference in nitrogen partial pressure across the membrane of thickness Δ_{mb}

$$n_{N_2,crs}(y) = -K_{N_2}(T,\lambda_{mb})(w_{an,ch} + w_{an,rib}) \times \frac{[P_{N_2,ca,mb}(y) - P_{N_2,an,mb}(y)]}{\Delta_{mb}} \qquad [8]$$

We assume that the permeation takes place both over the ribs and channels ($w_{an,ch} + w_{an,rib}$), where w_* indicates the width of each. The partial pressure of nitrogen at each membrane surface is calculated using the following expressions, $P_{N_2,an,mb}(y) = x_{N_2}(y)P_{an,in}$

Table III. Tuned parameters.

$i_{o,ref,ca}$	7×10^{-8} A cm^{-2}	Cathode exchange current
$i_{o,ref,an}$	0.05 A cm^{-2}	Anode exchange current
i_{loss}	1×10^{-3} A cm^{-2}	Crossover current
D_{eff}	0.35	Effective diffusivity in GDL
R_{GDL}	0.275 Ω cm^2	Contract resistance
α_{N_2}	2	N_2 perm scale factor

and $P_{N_2,ca,mb}(y) = P_{ca,in} - P_v(T) - P_{O_2,ca,mb}(y)$, assuming uniform pressure and saturated water vapor everywhere. This is reasonable, considering the water generation rate, especially when humidified inlets are used at low to mid temperatures. The oxygen concentration at the cathode surface of the membrane, $P_{O_2,ca,mb}(y)$, is calculated using Eq. 26. The nitrogen permeation rate, $K_{N_2}(T,\lambda_{mb})$, is given by Eq. 30, and depends both on temperature and membrane water content.

The hydrogen reaction rate is calculated from the local current density

$$n_{H_2,rct}(y) = \frac{i_{fc}(y)}{2F}(w_{an,ch} + w_{an,rib}) \quad [9]$$

where F is Faraday's constant.

The source term for water vapor in the AN CH is also membrane crossover, which is calculated from the diffusion and electro-osmotic drag

$$n_{H_2O,crs} = -\left[\frac{\lambda_{ca} - \lambda_{an}}{R_{w,mb}} - n_d(\lambda_{mb})\frac{i_{fc}}{F}\right](w_{an,ch} + w_{an,rib}) \quad [10]$$

where $R_{w,mb}$ is the resistance to membrane transport

$$R_{w,mb} = \frac{\Delta_{mb}}{D_w(\lambda_{mb},T)} + \frac{1}{k_{ads}} + \frac{1}{k_{des}} \quad [11]$$

arising from diffusion, where $D_w(\lambda_{mb},T)$ is the water diffusion coefficient for water in the membrane[26] and interfacial mass transfer attributed to membrane adsorption k_{ads} and desorption k_{des}.[26-28] The coefficient of electro-osmotic drag, $n_d(\lambda_{mb})$, can also be found in Ref. 26. Both D_w and n_d are λ_{mb}-dependent and increase with membrane water content.

The membrane water content is the final dynamic state in the model and is calculated from the difference between the anode and cathode equilibrium lambda values

$$\frac{\partial \lambda_{mb}(y)}{\partial t} = K_{mb}[\lambda_{an}(y) + \lambda_{ca}(y) - 2\lambda_{mb}(y)] \quad [12]$$

where $K_{mb} = k_{ads}/A_{mb} = 0.25$ is the membrane water uptake rate. Other, more recent models for membrane water uptake[27,28] will be investigated in a future work but should not impact the results for nitrogen accumulation presented here.

The equilibrium membrane water content is calculated from the water activity using the uptake isotherm[26]

$$\lambda_{an}(y) = c_0(T) + c_1(T)a_{H_2O,an} + c_2(T)a^2_{H_2O,an} + c_3(T)a^3_{H_2O,an} \quad [13]$$

where $a_{H_2O,an}(y) = x_{H_2O}(y)P_{an,in}/P_{sat}(T)$.

There exists a coupling between membrane water content, $\lambda_{mb}(y)$, the current density distribution, $i_{fc}(y)$, and nitrogen crossover rate, $K_{N_2}(T,\lambda_{mb})$. The nitrogen permeation rate depends on membrane water content, and the nitrogen accumulation rate depends on both the permeation rate and current density distribution (convective vs diffusive flow). The current density distribution depends on nitrogen accumulation (through blanketing of H_2) and the membrane water content for proton transport losses in the membrane. Finally, the membrane water content depends on the local current density and channel/GDL conditions.

Modeling the GC sample location.— The flow of gas removed from the AN CH during sampling is modeled by modifying Eq. 7 to include the sample flow

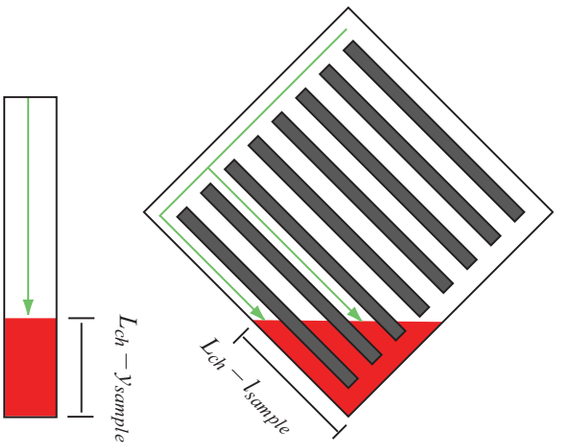

Figure 7. (Color online) Mapping AN CHs to equivalent single channel. The path length, in the 45° orientation, to nitrogen front location is the same for all channels.

$$N_t(y) = N_t(L) + \int_y^L [n_{H_2,rct}(\tilde{y}) + n_{N_2,crs}(\tilde{y}) + n_{H_2O,crs}(\tilde{y})]d\tilde{y} + \begin{cases} N_{sample} & \text{for } (y \le y_{sample}) \\ 0 & \text{for } (y > y_{sample}) \end{cases} \quad [14]$$

where y_{sample} is the location of the sampling port along the equivalent channel.

Because the FC is on a 45° angle and each of the AN CHs is connected at the top and bottom, as shown in Fig. 1, the N_2 blanketing front propagation needs to be transformed for comparison with an equivalent straight single channel. The nitrogen coverage area, however, can be directly related to the coverage area in the single channel equivalent model. Hence, we use the following relationship for the virtual single channel FC sampling location y_{sample}

$$\frac{(L_{ch} - y_{sample})}{L_{ch}} = \frac{(L_{ch} - l_{sample})^2}{2A_{fc}} \quad [15]$$

This equation relates the fractional area below the sampling location for the FC placed in the diagonal orientation (right), as shown in Fig. 7, to the fractional area below the sampling location in the equivalent model (left), as shown in Fig. 6. The physical nitrogen sampling location is 3 cm from the bottom edge of the FC along the last channel, $L_{ch} - l_{sample} = 0.03$, as shown in Fig. 7.

Distributed current density.— In a previous work, the voltage was calculated based on a uniform apparent current density,[29] which is related to the catalyst area with sufficient reactants to support the reaction, i.e., the channel length not covered by nitrogen[3] or water.[29] In this work, we consider the distributed current density, which is calculated directly from the reactant concentrations. Although the apparent area modeling technique captured the correct voltage output behavior of the system, the full distributed current density approach is chosen for this work to match internal model states and the measurement of nitrogen molar fraction during sampling from the AN CH at the fixed sampling location (l_{sample}). The diffusion of hydrogen and nitrogen in the AN CH affects both the current density distribution and GC measurement.

The inputs to the voltage model are total current I_{fc}(A), temperature T(K), membrane water content distribution $\lambda_{mb}(y)$, hydrogen partial pressure at the membrane surface $P_{H_2,an,mb}(y) = RTc_{H_2,an,mb}(y)$ (Pa), and oxygen partial pressure at the cathode membrane surface $P_{O_2,ca,mb}(y)$ (Pa), which is calculated in Eq. 26. The cell terminal voltage is calculated from the open-circuit potential minus the concentration, overpotential, and ohmic losses

$$E_{cell} = E_{rev}(y) - \eta_{mb}(y) - \eta_{GDL}(y) - \eta_{act,ca}(y) - \eta_{act,an}(y) \quad [16]$$

The calculation of the FC terminal voltage and current density distribution requires the additional computation effort to solve $N + 1$ simultaneous nonlinear algebraic constraint equations, where N is the number of discretized sections used to solve the partial differential equation (PDE) system. The distributed current density is resolved by solving the set of N (Eq. 16) for a uniform potential E_{cell} and one equation for the conservation of current

$$\frac{I_{fc}}{A_{fc}} = \frac{1}{L_{ch}} \int_0^{L_{ch}} i_{fc}(y) dy \quad [17]$$

The reversible voltage is given by

$$E_{rev}(y) = E_0 - \frac{RT}{nF} \log \left\{ \frac{aH_2O(y)}{aH_2(y)\sqrt{[aO_2(y)]}} \right\} \quad [18]$$

where $E_0 = 1.229 - (T - T_0)2.304 \times 10^{-4}$.[30] The reactant and product activities are calculated from the concentrations $aH_2(y) = c_{H_2,an,mb}(y)/C_{ref,H_2}$, $aO_2(y) = c_{O_2,ca,mb}(y)/C_{ref,O_2}$, and $aH_2O = 1$ because the liquid water product is assumed. The subscript ref refers to the reference quantity, and subscript ca,mb refers to the cathode membrane surface.

To simplify the calculation of cell voltage, a hyperbolic sine function is used for the calculation of overpotentials, $\eta_{act,ca}$ and $\eta_{act,an}$, from the exchange current density, $i_{o,ca}(y)$ and $i_{o,an}(y)$

$$\eta_{act,ca}(y) = \frac{RT}{\alpha_{c,a} nF} a \ \sinh\left[\frac{k_{units} i_{fc}(y) + i_{loss}}{2 i_{o,ca}(y)} \right] \quad [19]$$

where $k_{units} = 100^{-2}$ m^2/cm^2 is for units conversion, $i_{fc}(y)$ is the distributed current density from Eq. 17, and i_{loss} is the lost current density due to hydrogen crossover, a tuned parameter which is listed in Table III. The hyperbolic sine is equivalent to the Butler–Volmer equation when the forward and reverse reaction coefficients ($\alpha_{c,a} = \alpha_{c,c}$) are equal.[31]

Although the cathode reaction depends on the oxygen concentration as well as the activity of protons in the membrane,[32] the proton activity term is typically neglected because there are sufficiently many protons under the FC normal operation. Because we expect a low hydrogen concentration in the anode near the end of the channel, we include the proton effect on the exchange current density

$$i_{o,ca}(y) = i_{o,ref,ca} \left[\frac{c_{O_2,ca,mb}(y)}{C_{ref,O_2}} \right]^{\gamma_{O_2}} \left[\frac{c_{H^+_{ca,mb}}(y)}{C_{ref,H^+}} \right]^{\gamma_{H^+}} \times \exp\left[\frac{-E_c}{R} \left(\frac{1}{T} - \frac{1}{T_0} \right) \right] \quad [20]$$

where $i_{o,ref,ca}$ is the reference current density, c_* is the reactant concentration, γ is the concentration parameter, and E_c in the Arrhenius term is the activation energy for hydrogen oxidation on platinum.[33] The cathode concentration parameter for the local proton activity ($\gamma_{H^+} = 0.5$) is given by Ref. 34. The inclusion of proton concentration is required to capture the effect of nitrogen blanketing in the AN CH, which prevents hydrogen from reaching the catalyst layer to supply protons for the reaction. The cathode exchange current density is proportional to the square root of the local proton activity at the cathode catalyst layer and the proton activity in the cathode catalyst layer depends on the concentration of protons dissolved in the aqueous phase in the membrane, which is proportional to the square root of the hydrogen pressure at the anode membrane surface for low P_{H_2};[35] therefore, we approximate this relationship with a hyperbolic tangent function

$$\left(\frac{c_{H^+_{ca,mb}}}{C_{ref,H^+}} \right)^{\gamma_{H^+}} = K_{H_2} \ \tanh\left(100 \frac{c_{H_2,an,mb}}{c_{ref,H_2}} \right) \quad [21]$$

The constant K_{H_2} is absorbed into the reference current density $i_{o,ref,ca}$. At the limit, when the hydrogen concentration is zero, the proton activity at the anode drops to zero. Thus, when the anode is subjected to local fuel starvation, the hydrogen partial pressure drops; hence, the proton concentration in the cathode decreases. Furthermore, the membrane electrolyte conductivity also decreases due to lower contribution from the proton conduction in the bulk phase akin to increasing electrolyte resistance due to decreasing ionic concentration.[32] The overall reduction of proton activity at the cathode ultimately leads to a drop in the local current density near the dead-ended exit of the anode. For constant load current (galvanostatic) conditions, as the power production near the outlet shuts down, the current density increases near the anode inlet, where the membrane is relatively dry, which may lead to higher losses and increased temperature.

Similarly, for the anode side

$$\eta_{act,an}(y) = \frac{RT}{\alpha_{a,a} nF} a \ \sinh\left[\frac{k_{units} i_{fc}(y) + i_{loss}}{2 i_{o,an}(y)} \right] \quad [22]$$

where the anode exchange current density is

$$i_{o,an} = i_{o,ref,an} \left(\frac{c_{H_2,an,mb}}{C_{ref,H_2}} \right)^{\gamma_{H_2}} \exp\left[\frac{-E_c}{R} \left(\frac{1}{T} - \frac{1}{T_0} \right) \right] \quad [23]$$

The membrane resistance is calculated as follows

$$\eta_{mb}(y) = \frac{k_{units} i_{fc}(y) \Delta_{mb}}{\sigma_{mb}(\lambda_{mb}, T) \tanh(100 c_{H_2,an,mb}/C_{ref,H_2})} \quad [24]$$

Again, the hyperbolic tangent is used to approximate the relationship between conductivity and proton concentration[35] and to reflect the effect of increasing electrolyte resistance due to decreasing ion concentration.[32] The membrane conductivity $\sigma_{mb}(\lambda_{mb}, T)$ is a function of water content using the standard relationship from Springer et al.[36]

Finally, the GDL and contact resistances are lumped into R_{GDL} for the ohmic loss term

$$\eta_{GDL}(y) = k_{units} i_{fc}(y) R_{GDL} \quad [25]$$

The voltage model was tuned using flow-through data from the FC then compared with the experimental voltage degradation rates under dead-ended operating conditions. For model tuning with flow-through data, it is assumed that the membrane is fully humidified $\lambda(y) = \lambda(T, a = 1)$, where $\lambda(T, a = 1)$ can be found in Ref. 37, and the effects of GDL and cathode catalyst layer flooding are ignored due to the low current density operation.

Along the channel distributions, because the oxygen partial pressure in the CA CH is not presently considered as one of the dynamic states in the model, it is calculated simultaneously with the current density distribution $i_{fc}(y)$ (A/cm^{-2}) from the cathode inlet pressure and SR using

$$P_{O_2,ca,mb}(y) = P_{O_2,ca,in} - \frac{RT}{4F} \left[\frac{i_{fc}(y)}{h_m} + \frac{i_{fc}(y) \Delta_{GDL}}{D_{O_2,eff}} + \int_0^y \frac{i_{fc}(\tilde{y})}{u_{ca,in} h_{ca,ch}} d\tilde{y} \right] \frac{(w_{ca,ch} + w_{ca,rib})}{(w_{ca,ch})} \quad [26]$$

where $h_{ca,ch}$ is the CA CH height, $w_{ca,ch}$ is the CA CH width, and $w_{ca,rib}$ is the cathode rib width. h_m is the interfacial mass-transfer coefficient,[31] and $u_{ca,in}$ is the cathode inlet gas velocity (assumed constant along the length of the CA CH for simplicity)

$$u_{\mathrm{ca,in}} = \frac{\mathrm{SR_{ca}} I_{\mathrm{fc}} (w_{\mathrm{ca,ch}} + w_{\mathrm{ca,rib}}) L_{\mathrm{ca,ch}} (RT)}{(4F) A_{\mathrm{fc}} P_{\mathrm{O_2,ca,in}} (h_{\mathrm{ca,ch}} w_{\mathrm{ca,ch}})} \quad [27]$$

where the partial pressure of oxygen at the cathode inlet is given by $P_{\mathrm{O_2,ca,in}} = \mathrm{OMF_{ca,in}}(P_{\mathrm{ca,in}} - P_{\mathrm{v,ca,in}})$. $P_{\mathrm{ca,in}}$ is the cathode inlet pressure, $P_{\mathrm{v,ca,in}}$ is the cathode inlet vapor pressure, and $\mathrm{OMF_{ca,in}} = 0.21$ is the oxygen molar fraction. $\mathrm{SR_{ca}}$ is the cathode stoichiometry.

The cathode vapor pressure along the length of the channel is calculated similarly

$$P_{\mathrm{H_2O,ca}}(y) \approx \min\left[P_{\mathrm{sat}}(T), P_{\mathrm{H_2O,ca,in}} + \frac{RT}{4F} \int_0^y \frac{i_{\mathrm{fc}}(\tilde{y})}{u_{\mathrm{ca,in}} h_{\mathrm{ca,ch}}} d\tilde{y} \frac{(w_{\mathrm{ca,ch}} + w_{\mathrm{ca,rib}})}{(w_{\mathrm{ca,ch}})} \right] \quad [28]$$

This equation actually needs $+\int n_{\mathrm{H_2O,crs}}(\tilde{y}) d\tilde{y}$ to be correct, but then it becomes difficult to solve for the steady-state cathode vapor distribution analytically. At high cathode SR, this should not be a problem, but it may affect the O_2 distribution in low SR; however, this still should be a second order effect compared to variations in the anode.

The AN CH hydrogen concentration is propagated to the membrane surface assuming a simple diffusion model

$$c_{\mathrm{H_2,an,mb}}(y) = \frac{x_{\mathrm{H_2}}(y) P_{\mathrm{an,ch}}}{RT} - \frac{i_{\mathrm{fc}}(y)}{2F} \frac{\Delta_{\mathrm{GDL}}}{D_{\mathrm{H_2,eff}}} \frac{(w_{\mathrm{an,ch}} + w_{\mathrm{an,rib}})}{w_{\mathrm{an,ch}}} \quad [29]$$

based on the effective diffusivity $D_{\mathrm{H_2,eff}} = D_{\mathrm{eff}} D_{\mathrm{H_2,N_2}}$.[38]

Nitrogen crossover rate.— Kocha et al.[4] reported a large range of nitrogen permeability, over 1 order of magnitude. The permeation increases with both membrane water content and temperature. Temperature has a larger effect on permeability when the membrane is well hydrated. In this case, the permeability can change by a factor of 2–5 over the normal range of operating temperatures 30–60°C. The nitrogen permeation model includes the effects of membrane water content and temperature[39]

$$K_{\mathrm{N_2}}(T, \lambda_{\mathrm{mb}}) = \alpha_{\mathrm{N_2}} (0.0295 + 1.21 f_{\mathrm{v}} - 1.93 f_{\mathrm{v}}^2) \times 10^{-14} \times \exp\left[\frac{E_{\mathrm{N_2}}}{R} \left(\frac{1}{T_{\mathrm{ref}}} - \frac{1}{T} \right) \right] \quad [30]$$

where $E_{\mathrm{N_2}} = 24{,}000$ J mol^{-1}, $T_{\mathrm{ref}} = 303$, R is the universal gas constant, and f_{v} is the volume fraction of water in the membrane given by

$$f_{\mathrm{v}} = \frac{\lambda_{\mathrm{mb}} V_{\mathrm{w}}}{V_{\mathrm{mb}} + \lambda_{\mathrm{mb}} V_{\mathrm{w}}} \quad [31]$$

where $V_{\mathrm{mb}} = \mathrm{EW}/\rho_{\mathrm{mb,dry}}$ is the dry membrane volume, equivalent weight divided by density, and V_w is the molar volume of water. λ_{mb} is the membrane water content.

A change in permeability could account for the different nitrogen accumulation rates observed via different voltage drop rates, assuming the voltage degradation is caused by nitrogen accumulation. The current density would tend to shift toward the inlet, where the membrane is dry and has lower proton conductivity; hence, there would be increased resistive losses when N_2 accumulates in the end of the channel.

Modeling Results

The PDE (Eq. 1) is discretized using a central difference in space into $N = 50$ sections and solved using an ode solver. The AN CH model is solved using MATLAB "ode15s," which supports differential algebraic equations of the form

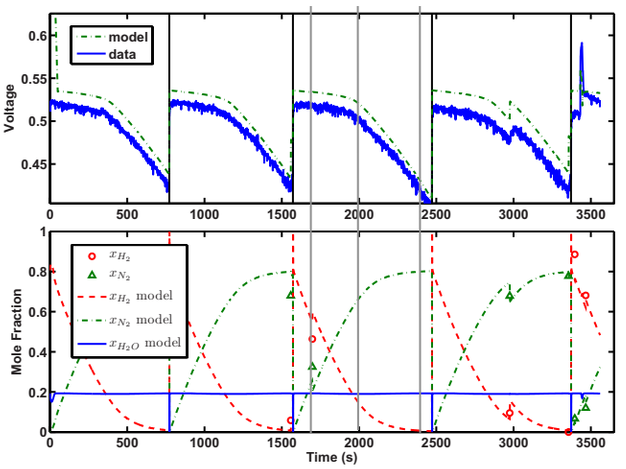

Figure 8. (Color online) Operating condition 3 (*i*0.6 _ T65 _ SR2 _ RH60) shows very good results with model matching because the assumption of nonwater plugging conditions in the channels is satisfied.

$$M\dot{z} = f(z) \quad [32]$$

where $z = [x_{\mathrm{N_2,an}}, x_{\mathrm{H_2O,an}}, \lambda_{\mathrm{mb}}, i_{\mathrm{fc}}, E_{\mathrm{cell}}]^T$, $M = \mathrm{diag}(I^N, I^N, I^N, 0^N, 0)$, and I^N is the $N \times N$ identity matrix.

Three simulation plots are shown in Fig. 8, 10, and 11, corresponding to operating conditions 3, 5, and 6, respectively. These portions of data are contained within the large data sets shown in Fig. 3 and 4. The first two data sets are chosen to match the model assumptions of humidified channel conditions but no channel liquid water plugging. The third condition shows some flooding and hence error in the model prediction of voltage, but the overall dynamic voltage behavior is captured quite well by the model ignoring the offset. The first plot in Fig. 8 corresponding to condition 3 shows the measured and predicted voltage in the top subplot and the GC measurement and simulated mole fraction at the sampling location in the bottom subplot. The model agrees very well with the data at this operating condition because no AN CH liquid water accumulation was observed during this period. Figure 9 shows the time evolution

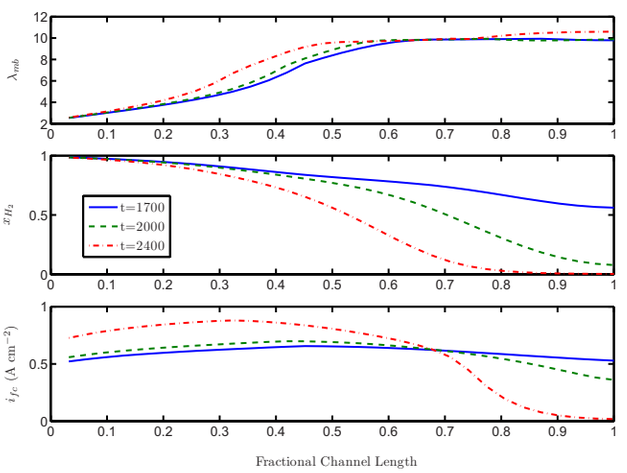

Figure 9. (Color online) The first subplot shows a snapshot of the membrane water content along the length of the channel for three times, as shown in Fig. 8; after a purge, midcycle, and before the next purge. The second subplot shows the hydrogen mole fraction along the length of the channel. The final subplot shows the current density distributions. The front is fully developed at $t = 2400$ s, leading to hydrogen starved region covering nearly 20% of the channel.

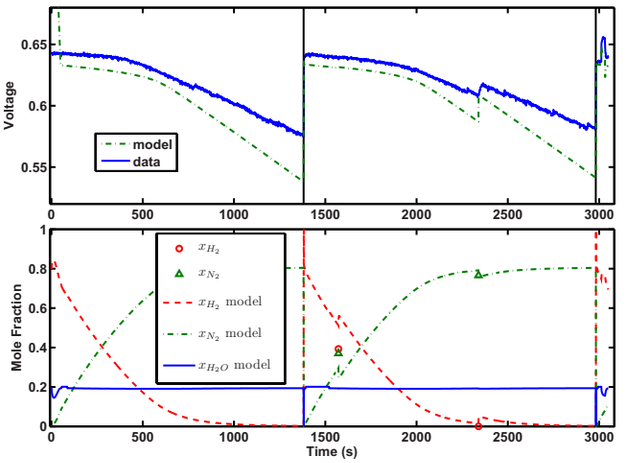

Figure 10. (Color online) Operating condition 5 (*i*0.4 _ T60 _ SR3 _ RH60).

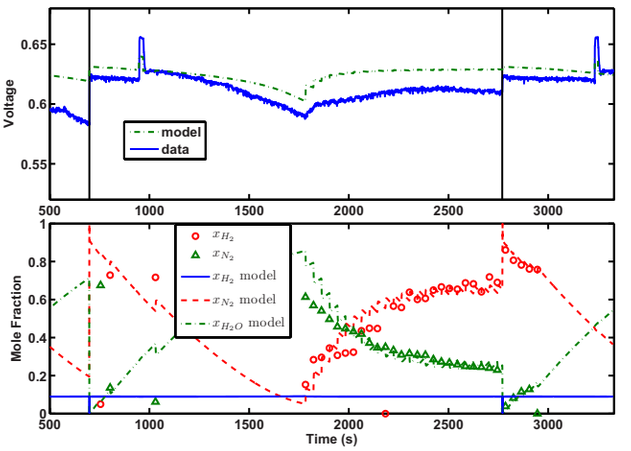

Figure 11. (Color online) Operating condition 6 (*i*0.4 _ T50 _ SR3 _ RH90): Good agreement with nitrogen measurement during continuous sampling but poor voltage model matching because flooding effects are not included in the voltage model.

of the hydrogen mole fraction distribution and membrane water content over a purge cycle. Three snapshots of the distributions, corresponding to $t = 1700$ s, $t = 2000$ s, and $t = 2400$ s, from the third cycle in Fig. 8 are shown. The "corner" in the voltage trace at $t = 2000$ s, where the rate of voltage degradation increases, indicates that a sufficient amount of nitrogen has accumulated in the channel to create a stratified front and a hydrogen starved region develops at the outlet. Finally, at $t = 2400$ s, the nitrogen front has evolved to cover nearly 20% of the AN CH. At this time, the effect of nitrogen blanketing is clear as the current density (the dashed-dotted line in the third subplot) is shifted.

Operating condition 5 shown in Fig. 10 corresponds to higher cathode stoichiometry and lower current density; therefore, we see slightly drier conditions along the channel but very similar membrane water content behavior to the previous case. The corner in the voltage model occurs too late, which indicates that either the diffusion coefficient is too large or the nitrogen accumulation rate is too low and the membrane resistance is too high because the voltage degradation rate after the corner point is too steep. Notice the effect of GC sampling on voltage for the samples that occur early in the purge cycle compared to those that occur later (larger voltage recovery), which the model accurately predicts.

Figure 11 shows a good match with the GC measurement for repeated sampling. This data set corresponds to lower operating temperature and fully humidified cathode inlet conditions, which exhibit both anode and CA CH plugging, hence the discrepancy between the modeled and measured voltage. The voltage matching is not very good because the effects of flooding or plugging are not represented in the voltage model. Cathode flooding and plugging are responsible for almost 20 mV of voltage loss, which can be recovered by the cathode surges at $t = 1000$ s and $t = 3400$ s. The membrane water content distribution, shown in Fig. 12, is much more uniform due to the humidified cathode inlet conditions and does not change over the purge cycle as in the previous cases.

The parameters α_{N_2} and D_{H_2,N_2} affect the rate of nitrogen front propagation and the delay before the voltage decay changes slope, as seen in Fig. 8. Nitrogen front propagation is also weakly dependent on the current density distribution $i_{fc}(y)$ because the consumption of hydrogen drives convection in the channel. The slope of voltage drop depends on membrane/GDL resistance, the nitrogen diffusion rate, and the nitrogen front propagation speed.

Effect of operating conditions.— Figures 13 and 14 show the effects of increasing temperature and current density, respectively. Increasing temperature increases both permeation through the membrane and to a small extent diffusion. The increased nitrogen permeation rate leads to both a quicker formation of the nitrogen blanket, the time at which the voltage slope changes, and the faster propagation of the blanketing front, which can be seen in the steeper second slope of the voltage plot. The effect of current density is more difficult to visualize because the voltages are very different; therefore, the deviation from the nominal voltage for each given current density is plotted in the first subplot of Fig. 14. The second subplot shows the hydrogen and nitrogen mole fraction at the sampling location. Because the convective term in Eq. 1 is proportional to the current density, nitrogen is pushed toward the end of the channel more quickly with increasing current density. As a result, the blanketing front forms much more quickly at a high current density but the propagation rate of the front does not increase very much because the permeation rate is constant. This can be seen in the third subplot, which shows the average mole fraction of nitrogen in the AN CH, which is nearly identical for all four cases.

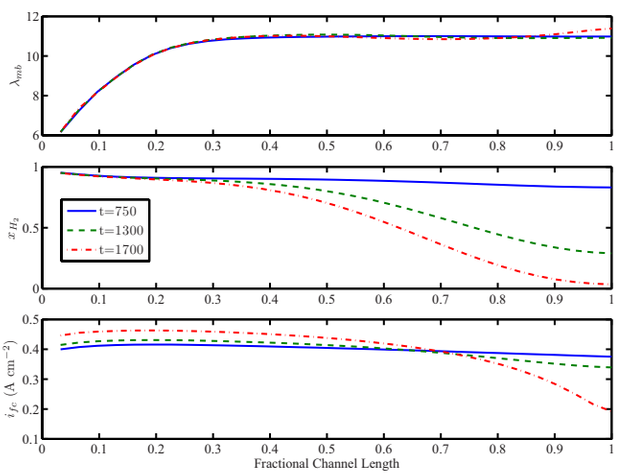

Figure 12. (Color online) The first subplot shows a snapshot of the membrane water content along the length of the channel for three times, as shown in Fig. 11; after a purge (before surge), midcycle, and before the next purge. The second subplot shows the hydrogen mole fraction along the length of the channel. The final subplot shows the current density distributions. Notice the different membrane profiles due to higher cathode inlet RH and less developed nitrogen front.

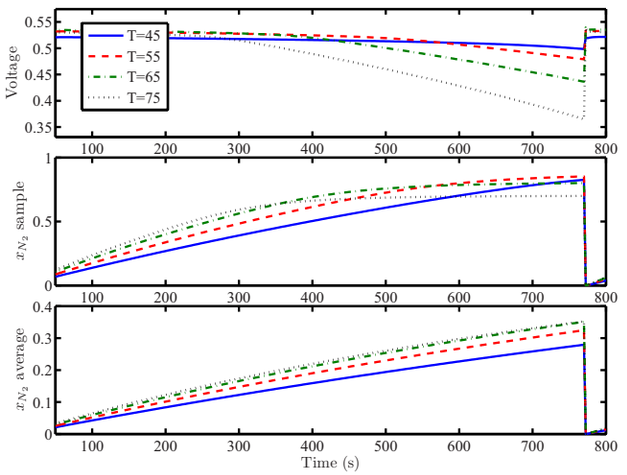

Figure 13. (Color online) Model temperature effects.

Conclusions

The one-dimensional AN CH model presented in this paper is able to capture and explain the observed two-sloped voltage drop between purges in a PEMFC with DEA. The model shows very good results when the assumption of nonwater plugging conditions are met in the channels. The evolution of a nitrogen blanketing front, which leads to a hydrogen depleted region in the AN CH, explains the voltage loss. Although distributed current density measurements[40,41] were not acquired, we can observe the effect of mass accumulation on current density distribution through the cell potential by measuring the terminal voltage. Specifically, the mass accumulation affects both the rate of voltage drop and the time at which the steeper slope begins.

The ability of the model to predict voltage is limited because the accumulation of liquid water in the AN CH (plugging) and cathode catalyst layer (flooding) are not included in the model, but the voltage degradation and nitrogen accumulation rates match well when the assumption of nonflooding and nonplugging conditions are valid. In the future, we plan to incorporate these effects into the model. The effects of nitrogen and liquid water accumulation can be parameterized by utilizing the measurement of liquid water from neutron imaging along with the GC measurements for combinations of wet and dry channel conditions. The data set corresponding to operating condition 6, shown Fig. 11, could be used for parameterizing the liquid water effect using the model of nitrogen accumulation, which is calibrated for drier (nonflooding/plugging) conditions.

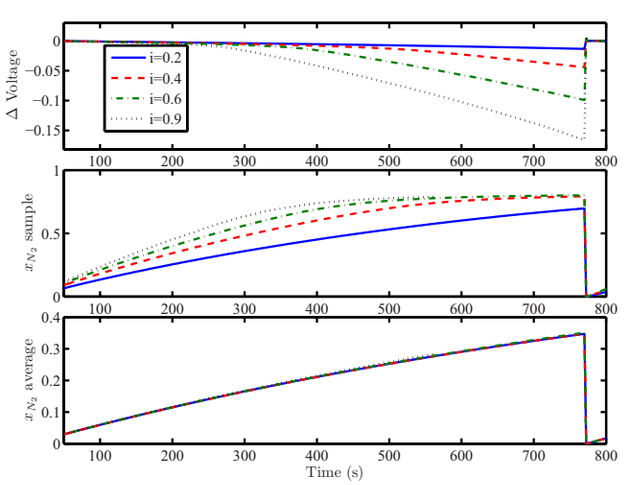

Figure 14. (Color online) Model current density effects.

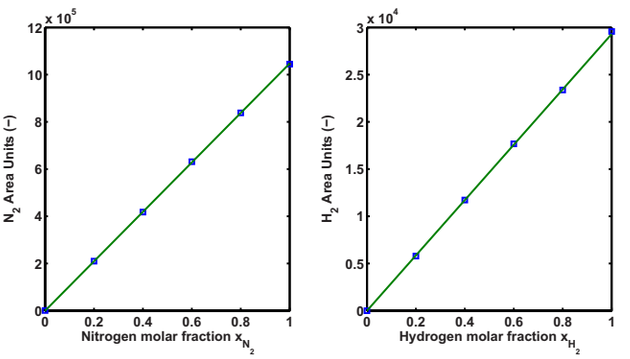

Figure 15. (Color online) GC calibration data.

Acknowledgments

This work was supported by The National Science Foundation through CBET-0932509 and the National Institute for Standards and Technology Center for Neutron Research (NCNR). James Marcicki assisted with the data collection. The authors are also grateful for the help they received collecting and analyzing data from Daniel S. Hussey and David L. Jacobson at the NCNR.

University of Michigan assisted in meeting the publication costs of this article.

Appendix: Nomenclature and Constants

GC calibration.— The injection port inside the GC was maintained at 100°C and the column at 30°C. A TCD was used for gas detection. The TCD was operated at 100°C and 90 mA current.

Two mass flow controllers were used to create dry gas mixtures of a known (H_2/N_2) concentration in the AN CH for the calibration of the GC detector. Calibration data were collected with the AN CH at 4.5 psig operating pressure and a nominal temperature of $T = 60$°C. A six-point calibration was used, with five samples repeated for each point. Figure 15 demonstrates the linearity of the GC measurement. The detector is much more sensitive to nitrogen due to the choice of carrier gas. The average N_2 response is 1,163,897 (area units/x_{N_2}), and the average hydrogen response is 24,416 (area units/x_{H_2}). Because the measurement of H_2O was not possible during FC operation, we assume that the concentration of vapor in the anode is equal to the saturation value and hence only temperature-dependent.

References

1. A. Karnik, J. Sun, and J. Buckland, in *American Control Conference*, American Automatic Council (AACC), p. 6 (2006).
2. R. K. Ahluwalia and X. Wang, *J. Power Sources*, **177**, 167 (2008).
3. E. A. Müller, F. Kolb, L. Guzzella, A. G. Stefanopoulou, and D. A. McKay, *J. Fuel Cell Sci. Technol.*, **7**, 021013 (2010).
4. S. S. Kocha, J. D. Yang, and J. S. Yi, *AIChE J.*, **52**, 1916 (2006).
5. A. Z. Weber, *J. Electrochem. Soc.*, **155**, B521 (2008).
6. J. B. Siegel, D. A. McKay, A. G. Stefanopoulou, D. S. Hussey, and D. L. Jacobson, *J. Electrochem. Soc.*, **155**, B1168 (2008).
7. C. A. Reiser, L. Bregoli, T. W. Patterson, J. S. Yi, J. D. Yang, M. L. Perry, and T. D. Jarvi, *Electrochem. Solid-State Lett.*, **8–6**, A273 (2005).
8. J. P. Meyers and R. M. Darling, *J. Electrochem. Soc.*, **153**, A1432 (2006).
9. R. Borup, J. Meyers, B. Pivovar, Y. S. Kim, R. Mukundan, N. Garland, D. Myers, M. Wilson, F. Garzon, D. Wood, et al., *Chem. Rev. (Washington, D.C.)*, **107**, 3904 (2007).
10. E. Kimball, T. Whitaker, Y. G. Kevrekidis, and J. B. Benziger, *AIChE J.*, **54**, 1313 (2008).
11. C. H. Woo and J. Benziger, *Chem. Eng. Sci.*, **62**, 957 (2007).
12. E. Kumbur, K. Sharp, and M. Mench, *J. Power Sources*, **161**, 333 (2006).
13. F. Y. Zhang, X. G. Yang, and C. Y. Wang, *J. Electrochem. Soc.*, **153**, A225 (2006).
14. J. Benziger, *AIChE J.*, **55**, 3034 (2009).
15. L. Dumercy, M.-C. Pra, R. Glises, D. Hissel, S. Hamandi, F. Badin, and J.-M. Kauffmann, *Fuel Cells*, **4**, 352 (2004).
16. W. Baumgartner, P. Parz, S. D. Fraser, E. Wallnöfer, and V. Hacker, *J. Power Sources*, **182**, 413 (2008).
17. S. Hikita, F. Nakatani, K. Yamane, and Y. Takagi, *JSAE Rev.*, **23**, 177 (2002).
18. H. Li, Y. Tang, Z. Wang, Z. Shi, S. Wu, D. Song, J. Zhang, K. Fatih, J. Zhang, H. Wang, et al., *J. Power Sources*, **178**, 103 (2008).
19. D. Hussey, D. Jacobson, and M. Arif, in *Proceedings of the ASME International Conference on Fuel Cell Science, Engineering and Technology*, ASME (2007).

20. D. Kramer, J. Zhang, R. Shimoi, E. Lehmann, A. Wokaun, K. Shinohara, and G. G. Scherer, *Electrochim. Acta*, **50**, 2603 (2005).
21. S. Basu, C.-Y. Wang, and K. S. Chen, *J. Electrochem. Soc.*, **156**, B748 (2009).
22. R. Fluckiger, S. A. Freunberger, D. Kramer, A. Wokaun, G. G. Scherer, and F. N. Buchi, *Electrochim. Acta*, **54**, 551 (2008).
23. P. Chang, G.-S. Kim, K. Promislow, and B. Wetton, *J. Comput. Phys.*, **223**, 797 (2007).
24. N. R. Amundson, T.-W. Pan, and V. I. Paulsen, *AIChE J.*, **49**, 813 (2003).
25. T. Berning and N. Djilali, *J. Electrochem. Soc.*, **150**, A1589 (2003).
26. S. Ge, X. Li, B. Yi, and I.-M. Hsing, *J. Electrochem. Soc.*, **152**, A1149 (2005).
27. M. Adachi, T. Navessin, Z. Xie, B. Frisken, and S. Holdcroft, *J. Electrochem. Soc.*, **156**, B782 (2009).
28. P. W. Majsztrik, M. B. Satterfield, A. B. Bocarsly, and J. B. Benziger, *J. Membr. Sci.*, **301**, 93 (2007).
29. D. A. McKay, J. B. Siegel, W. Ott, and A. G. Stefanopoulou, *J. Power Sources*, **178**, 207 (2008).
30. R. P. O'Hayre, S.-W. Cha, W. Colella, and F. B. Prinz, *Fuel Cell Fundamentals*, John Wiley & Sons, Hoboken, NJ (2006).
31. M. M. Mench, *Fuel Cell Engines*, John Wiley & Sons, Hoboken, NJ (2008).
32. J. S. Newman, *Electrochemical Systems*, 2nd ed., Prentice Hall, Englewood Cliffs, NJ (1991).
33. F. Barbir, *PEM Fuel Cells: Theory and Practice*, Elsevier, Burlington, MA (2005).
34. D. M. Bernardi and M. W. Verbrugge, *J. Electrochem. Soc.*, **139**, 2477 (1992).
35. A. Katsaounis, S. Balomenou, D. Tsiplakides, M. Tsampas, and C. Vayenas, *Electrochim. Acta*, **50**, 5132 (2005).
36. T. Springer, T. Zawodzinski, and S. Gottesfeld, *J. Electrochem. Soc.*, **138**, 2334 (1991).
37. J. B. Siegel, S. Yesilyurt, and A. G. Stefanopoulou, in *Proceedings of Fuel Cell 2009 Seventh International Fuel Cell Science, Engineering and Technology Conference*, ASME, p. 439 (2009).
38. J. Nam and M. Kaviany, *Int. J. Heat Mass Transfer*, **46**, 4595 (2003).
39. R. Ahluwalia and X. Wang, *J. Power Sources*, **171**, 63 (2007).
40. H. Ju and C. Wang, *J. Electrochem. Soc.*, **151**, A1954 (2004).
41. S. A. Freunberger, M. Reum, J. Evertz, A. Wokaun, and F. N. Buchi, *J. Electrochem. Soc.*, **153**, A2158 (2006).
42. R. Taylor and R. Krishna, *Multicomponent Mass Transfer*, John Wiley & Sons, New York (1993).